Journal of Petroleum Science and Engineering 181 (2019) 106229

Contents lists available at ScienceDirect

Journal of Petroleum Science and Engineering

journal homepage: www.elsevier.com/locate/petrol

Robust implementations of the 3D-EDFM algorithm for reservoir simulation with complicated hydraulic fractures

Cong Wang[a,b], Qiquan Ran[b], Yu-Shu Wu[a,*]

[a] Colorado School of Mines, USA
[b] Research Institute of Petroleum Exploration and Production, CNPC, China

ARTICLE INFO

Keywords:
Reservoir simulation
Fracture
Unconventional reservoirs
EDFM

ABSTRACT

The geometry of the subsurface hydraulic fracture is complicated which deviates from the conventional single pan shape. It can be in multi-wing shape by the formation heterogeneity and/or 3D fracture networks caused by the pre-exising natural fractures. Effective and flexible handling of hydraulic fractures is crucial for the reservoir simulation of unconventional reservoirs. In this paper, we discuss the robust implementations of the 3D-EDFM algorithm, which is applicable to numerical simulation of fluid flow in unconventional reservoirs with complicated, arbitrary 3D hydraulic fracture networks.

Key features of this 3D-EDFM methodology consist of vertex-based geometric calculations, and polygons with three to six vertices from box-plane intersections can be captured with this algorithm. The 3D-EDFM has been implemented in reservoir simulators via the integral finite difference (IFD) method. Its numerical scheme and implementation are verified by comparisons with analytical solutions and other established numerical solutions. This method not only provides an effective approach of handling realistic hydraulic fractures, but also significantly improves computational efficiency, while keeping sufficient accuracy. For some extreme cases that the transient state flow lasts long (i.e., large-size matrix blocks with extremely low permeability), our numerical analysis indicates only one level of local grid refinement (LGR) is needed to retain the required accuracy. We also provide an analytical-solution based method to optimize this LGR grid size if needed.

This enhanced method is able to handle multiple 3D hydraulic fractures with arbitrary strikes and dip angles, shapes, curvatures, conductivities, and connections. Therefore, the 3D-EDFM provides great flexibility to handle hydraulic-fracture input data, interpreted from geomechanics modelings as well as microseismic data, for reservoir simulation. We present illustrative application examples for three unconventional reservoir engineering problems of interest in practice: (1) a single fracture with a complicated shape due to multi-layer geological features, (2) multiple isolated fractures with curvatures due to the stress shadow effect, and (3) multiple fractures with complicated orientations caused by natural fracture interactions. The 3D-EDFM is demonstrated to capture all the key flow patterns dominated by the discrete fractures in these three cases.

1. Introduction

Numerical simulation is a widely practiced and accepted technique in reservoir engineering to study flow and transport processes in subsurface systems. It helps reservoir development and management by forecasting fluid production, optimizing well design and completion, identifying the needs of artificial lift at present or in future, and evaluating options of improved or enhanced oil recovery approaches. For unconventional reservoirs, however, there are some limitations on applications of reservoir simulation technology, and current understandings and reservoir simulation technologies used in this area are far behind industry needs. One of the major limitations is effective and flexible handling of hydraulic fractures, which are well-known to be crucial to hydrocarbon production from unconventional reservoirs, because they provide a high conductivity pathway for fluid flow from the tight matrix to producing wells. These hydraulic fractures will most likely deviate from conventional bi-wing, ideal planar patterns and have a more complex geometry, due to formation heterogeneities, stress shadow effect, and interactions with natural fractures.

Several methods have been developed and applied to quantify flow and transport in the porous medium with fractures. The first methodology is to represent the rock as dual continua (Warren and Root, 1963; Kazemi, 1969; Duguid and Lee, 1977; Pruess, 1985; Wu and Pruess, 1988). The dual-continuum approach is applicable to a

* Corresponding author.
E-mail addresses: congwang05@petrochina.com.cn (C. Wang), ywu@mines.edu (Y.-S. Wu).

https://doi.org/10.1016/j.petrol.2019.106229
Received 20 March 2018; Received in revised form 31 May 2019; Accepted 1 July 2019
Available online 03 July 2019
0920-4105/ © 2019 Published by Elsevier B.V.

Nomenclature

A_f = Section area of a fracture, L2
a, b, c, D, E = 3D plane parameters
d = distance, L
$\mathbf{e}_{\overrightarrow{ij}}$ = vector from 3D point i to j
FI = fracture index, L
k = absolution permeability, L2
k_r = relative permeability
$\hat{\mathbf{n}}$ = the unit normal vector
p = fluid pressure, m/Lt2
$\mathbf{P}$ = 3D point coordinates
q = volumetric flow rate, L3/t
Q_i = volumetric rate in element i; L3/t
S_β = liquid saturation of β-phase
t = time, t
T = single-variable function of t
V_i = volume of element i, L3
$\mathbf{V_i}$, $\mathbf{V}_j$ = coordinates of a 3D point
w_f = fracture width, L
x, y, z = 3D coordinates
X = single-variable function of x
x_f = fracture half-length, L
α = weight coefficient
φ = porosity
Φ = flow potential, m/Lt2
μ_β = viscosity of β-phase, m/Lt
λ = constant for convention
ρ_β = mass density of β-phase, m/L3

naturally fractured reservoir with a denser fracture network or under the condition that fractures can be represented as a continuum. It includes one rock matrix continuum (high storage capacity and low conductivity) and another overlapping fracture continuum (negligible storage capacity and high conductivity). Interactions between these two continua are accounted by fluid flow assumed at quasi-steady state under pressure differences. The double-porosity model assumes global flow only occurs in the fracture continuum, and the matrix continuum supports fractures locally. The dual permeability model, which is a more general version, accounts both fracture and matrix global connections.

Only two parameters (one governing inter-porosity flow and the other relating to matrix storage capacity) are additionally introduced in this dual-continuum method for fractures. These two parameters are typically inferred from the build-up well test by assuming fractures uniformly distributed in the reservoir scale (Warren and Root, 1963; Neuman, 2005). Hence this approach will inevitably miss some local dominant, discrete features, e.g., hydraulic fractures in unconventional reservoirs. The second approach (discrete fracture method, DFM for short), which can capture these local dominant features, is thus widely used to handle hydraulic fractures.

The DFM is to depict a reservoir system as a network of discrete fractures together with the permeable or impermeable matrix. This method directly makes use of fracture geometry data by considering fracture locations, orientations, shapes, apertures, and sizes. Numerically, fractures are explicitly modeled using specifically designed grid systems. The first gridding approach refines structured grids intersected by fractures at the scale of fracture widths. Fractures are then represented by a set of small-size and high-permeability grids (Slough et al., 1999; Sadrpanah et al., 2006). This local grid refinement (LGR) method can reduce numerical errors to an acceptable level. However, the substantial differences or highly contrasting respect ratios between adjacent grids regarding their dimensions can lead to numerical convergence problems. To overcome this problem, an approach of combining regular size grid and “pseudoized” fracture permeability is proposed, making the fracture conductivity (the multiplication between the fracture permeability k_f and the fracture aperture A_f) in the simulation identical to the real fracture conductivity (Rubin, 2010; Ding et al., 2014).

The second DFM approach is based on unstructured grids. The space domain is gridded by treating fractures as internal boundaries. To conform the fracture geometries, triangle or PEBI grids are used for 2D simulations (Karimi-Fard et al., 2004; Sun and Schechter 2014), and 3D tetrahedral grids (Hui et al., 2007) are used for 3D simulations. Compared with the LGR method, this approach is more flexible to handle fractures with arbitrary directions. However, constructing such meshes is quite challenging, especially, in three-dimensional problems considering multiple connected fractures, because the mesh has to be built in a way that the grid edges/faces coincide with all fracture surfaces.

The EDFM is another numerical technique of the generalized discrete fracture method. This method is first introduced by Lee et al. (Lee et al., 2001) to simulate long fractures and further extended by Li and Lee, (2008) and Moinfar (Moinfar et al., 2014). As its name implies, fractures are virtually embedded into the nearby matrix grid blocks. The fracture thickness is only considered in the computation domain for fracture volume calculations, but not represented in the grid domain, because fracture thickness is several orders of magnitude smaller than a typical simulation grid size.

As an analogy, the idea of the EDFM is similar to the well handling method in traditional reservoir simulation (Peaceman, 1978). This way, the mesh does not need to be specially processed to track the fracture path, which greatly reduces the number of grid cells and generate a Jacobian matrix with a similar sparsity pattern as the traditional reservoir simulation. Such features can significantly improve simulation efficiency. Because localized features are not efficiently resolved by its mesh refinement, this method cannot avoid introducing numerical discretization errors in the local approximation space domain. To resolve the problem, accuracy evaluation is one of focus points in this study.

This paper summarizes our recent study of enhancing the EDFM to model fluid flow in unconventional reservoirs with arbitrary 3D hydraulic fractures. In particular, we develop a vertex-based geometric algorithm to evaluate key parameters in the EDFM - the fracture index. It is able to handle multiple 3D hydraulic fractures with arbitrary strike and dip angles, shapes, conductivities, and connections. Its numerical implementation is verified by comparison with both analytical solutions and other established numerical solutions. In addition, our analytical and simulation results conclude the EDFM can provide results with acceptable accuracy for practical engineering applications. For some extreme cases that the transient state flow lasts long (large-size matrix grids with extremely low permeability), only one level of local grid refinement is needed to guarantee accuracy. We provide an analytical solution based approach to optimize this grid size, if local grid refining is needed. To illustrate this new approach, we present several application examples of interest to unconventional reservoir simulation. We demonstrate that the 3D EDFM is capable of handling common problems in unconventional reservoirs with complicated fractures, caused by multi-scale heterogeneity, stress shadow effect, and interactions between hydraulic and natural fractures.

2. Governing equations

In our previous work, we introduced a generalized framework model to simulate fluid flows in unconventional reservoirs (Wu, 1998; Wang, 2013; Wu et al., 2014; Wang and Wu, 2015; Cai et al., 2015). The integral finite difference method (equivalent to the Finite Volume

method) is chosen to discretize governing PDEs in the space domain (Narasimhan and Witherspoon, 1976; Pruess et al., 1999). Two types of equations in this method will be briefly discussed in this section, because both are involved with geometric quantities. The first group is the discrete equation for mass conservation of multiphase, multi-component fluid flow at grid block or node i, which can be written in a general form (Wu, 1998).

$$\left\{(\varphi S_\beta \rho_\beta)_i^{k,n+1} - (\varphi S_\beta \rho_\beta)_i^{k,n}\right\}\frac{V_i}{\Delta t} = \sum_{j\in\eta_i} flow_{ij}^{k,n+1} + Q_i^{k,n+1}(k = 1,2,3)\ and\ (i = 1,2,3,...,N) \tag{1}$$

where φ is the effective porosity of porous or fractured media; S_β and ρ_β are the saturation and density of fluid β; superscript k serves as an equation index for various phases with k = 1 (gas), 2 (water), and 3 (oil); superscript n and n+1 denote the previous time level and the current time level; subscript i is the index of grid block i; N is the total number of nodes or grid blocks; Δt is time step size; V_i is the node i volume; η_i contains neighboring nodes (j) of node i; the component mass "flow" term between node i and j are further explained in Eq. (2); Q is the sink/source term at node i for phase k.

The second set of equation is the expanded form of the flow term in the right-hand side of Eq. (1). It represents the mass flux by multiphase flow or advective processes mainly, which are described by a discrete version of Darcy's law or various non-Darcy flow models (Wu, 2002). When Darcy's law applies, the mass flux of fluid phase β along the connection in discrete mass conservation Eq. (1) is given by

$$flow_{\beta,ij} = \left(\frac{\rho_\beta k_{r\beta}}{\mu_\beta}\right)_{ij+1/2} \frac{A_{ij}\, k_{ij+1/2}}{d_i + d_j}(\Phi_{\beta j} - \Phi_{\beta i}) \tag{2}$$

where $k_{r\beta}$ and μ_β are the relative permeability and viscosity of fluid β; A_{ij} is the node i and j common interface area; d_i is the distance between the center of block i and the common interface A_{ij}. $k_{ij+1/2}$ is an averaged (such as harmonic-weighted) absolute permeability. $\Phi_{\beta j}$ is the flow potential of fluid β in node j.

Three geometric quantities involved in these two sets of equations are the element volume V_i, the connection area A_{ij}, and the connection distances d_i, d_j. One attractive feature of the IFD method is that these geometric quantities are input directly instead of having them generated during the simulation. Therefore, great flexibility is achieved so that a computational volume element in any one continuum (fracture or matrix) can connect with another element in its own or other continuum. In other words, no specific programming changes are required in the simulator to distinguish fracture-fracture, matrix-matrix, and fracture-matrix connections. All these different types of connections are handled numerically in the same way once their geometric properties are prepared and defined in the input file.

From this point of view, the IFD (or FV) is general for implementing various conceptual models of fractured reservoirs, which includes the classical dual-porosity and dual-permeability model, multiple interacting continua (MINC) model, discrete fracture model (DFM), and embedded discrete fracture model (EDFM). Therefore, the hybrid fracture model, which combines DFM, MINC, and a homogeneous porous medium, can be handled straightforwardly (Pruess, 1985). The key is obtaining geometric features or properties (volume, distance, and interface area) based on the model approximations and assumptions.

3. Geometric property calculation

The method of the 3D-EDFM is conceptually similar to 2D cases (Lee et al., 2001; Li and Lee, 2008; Yan et al., 2016), of which the key is the appropriate preprocessing of geometrical information. But its practical implementation is more complicated. As shown in Fig. 1, one full intersection between a box and a 3D plane could lead to a polygon with 3–6 vertices, not to mention if the plane partly penetrates the box, which makes the geometric calculation more complicated. In this section, some key geometry issues are described, aiming towards an accurate and robust implementation for multiple fractures with arbitrary shapes, directions, conductivities and connections.

3.1. Connection area

Our approach of computing the area of intersection polygons is based directly on vertices, which includes three major steps: 1) finding all vertices of the intersected polygon; 2) sorting all these vertices in the clockwise or counter-clockwise order; and 3) calculating the intersected polygon area based on the well-sorted vertices; To obtain all intersections in a fractured reservoir, we need to calculate the intersection between each fracture and each grid cell first, which starts from finding all vertices of the intersected polygon by checking:

1. if one or more of the fracture polygon points are inside the box;
2. if any of the box edges are intersected with the fracture polygon face; and
3. if any of the fracture polygon's edges are intersected with the box faces.

Once the vertex coordinate array and the vertex order are prepared, the area of the intersected polygon can be calculated by summing up a series of triangle areas.

$$A_{polygon} = \sum_{i=1}^{n} \Delta CE_i \tag{3}$$

where n is the number of polygon edges; C is the central point of the polygon; E is the ith edge of the polygon.

3.2. Connection distances

In this numerical method, the distance from the center of a fracture element to the fracture-matrix interface is set to zero, because the fracture width or aperture is negligible compared with a typical matrix block size, and the pressure within the fracture grid reaches equilibrium in the perpendicular direction to the fracture plane almost instantaneously. The distance from the computational center of the matrix element to the common interface is estimated by the numerical

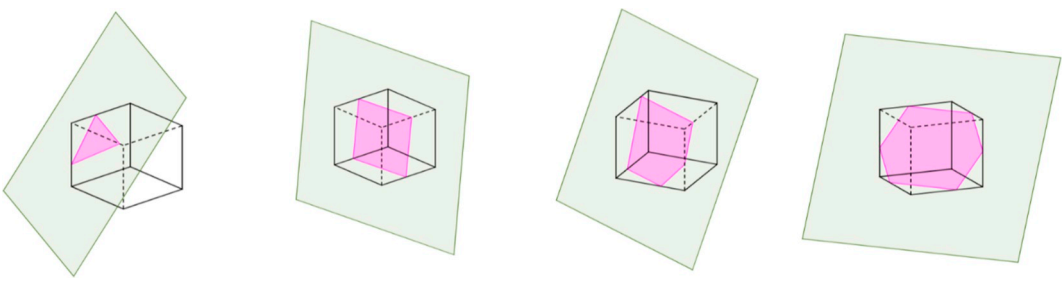

Fig. 1. Schematic of the full intersection between a box and a fracture plane, leading to a polygon with 3–6 vertices.

integration over the grid volume.

It can be proven that this geometrical average distance equals to the fluid-flow average distance if flow inside the intersected grid block is in the steady and pseudo-steady state (Appendix B). However, if fluid flow is in the transient state (e.g. only part of the grid volume is drained), the geometrical average distance cannot represent the fluid-flow average distance anymore. This situation usually happens at the beginning of productions or injections. A substantial amount of simulation errors can be expected if this transient-state situation lasts long, which possibly occurs for cases with large-size matrix blocks with extremely low matrix permeability. To quantify this effect and to optimize grid-block sizes for the EDFM, analytical solutions of a 1D fluid flow problem with single fracture are derived.

In the 1D problem, constant fracture pressure is applied on the right (Dirichlet condition), and closed boundary condition is applied on the left (Neumann condition). Eq. (4) gives its analytical solution. Details about the derivation are included in Appendix A.

$$p(x,t) = p_f + \frac{2(p_i - p_f)}{\pi}\sum_{n=1}^{\infty}\frac{1}{\left(n-\frac{1}{2}\right)}\sin\left[\left(n-\frac{1}{2}\right)\pi\frac{x}{x_L}\right]\exp\left(-(n-0.5)^2\pi^2\frac{k}{\varphi\mu c x_L^2}t\right) \tag{4}$$

The geometrical average distance (d_{m-g}) for the fracture-intersected grid block (the first grid block in this problem) is half of the grid size. The fluid-flow average distance (d_{m-f}) is derived based on the analytical solution.

$$d_{m-g} = \frac{\Delta x_1}{2} \tag{5}$$

$$d_{m-f} = \frac{x_L^2\sum_{n=1}^{\infty}\frac{1}{(n-0.5)^2}\left(1-\cos\left[(n-0.5)\pi\frac{\Delta x_1}{x_L}\right]\right)\exp\left(-(n-0.5)^2\pi^2\frac{k}{\varphi\mu c x_L^2}t\right)}{\Delta x_1\pi^2\sum_{n=1}^{\infty}\exp\left(-(n-0.5)^2\pi^2\frac{k}{\varphi\mu c x_L^2}t\right)} \tag{6}$$

where the average distance d_{m-f} is a function of grid block size Δx_1, reservoir/matrix permeability k, reservoir/matrix porosity φ, fluid viscosity μ, total compressibility c, time t, and reservoir size x_L. Further analysis indicates that d_{m-f} is most sensitive to reservoir/matrix permeability, grid block size, and time among all these parameters within physically reasonable ranges. We plot the ratio of these two average distances as a function of time with two different permeability (1.0 mD and 0.01 mD) and three different matrix grid-block sizes (1 m, 5 m, and 10 m), as shown in Fig. 2. For the matrix permeability of 1.0md, the geometrically calculated average distance with these three grid-block sizes is close to the analytically derived distance in early-, mid-, and late-stages. This means the numerical solution from the EDFM method will be in good agreement with the analytical (true) solution. For the permeability of 0.01 mD, however, cases with 5 m and 10 m blocks have a considerable discrepancy before 1.0 day. Numerical solutions with the EDFM method will have substantial errors in the early time correspondingly. The case with the 1 m grid keeps close almost all the

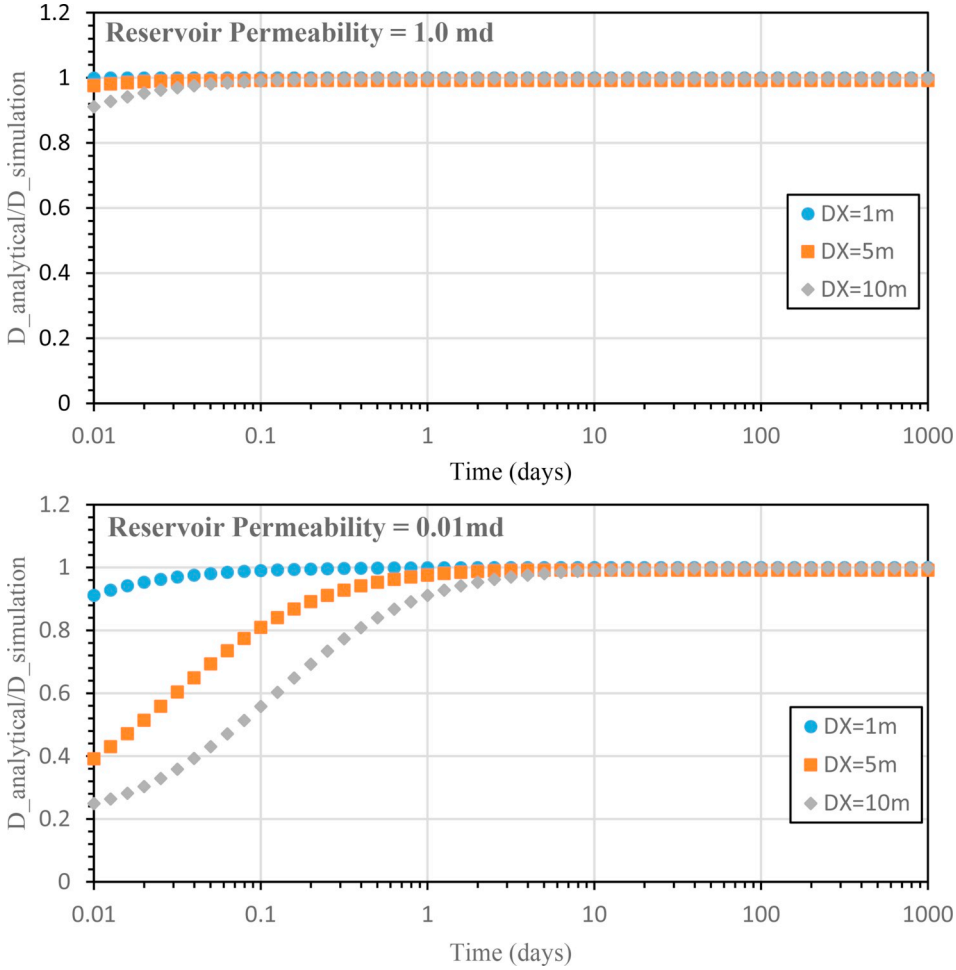

Fig. 2. Ratio of two average distances with time for two different matrix permeability (1.0 mD and 0.01 mD) and three different matrix-block sizes (1 m, 5 m, and 10 m).

time.

Quantitative studies above indicate that the EDFM does not guarantee to provide accurate solutions under all conditions, which can be verified by simulation results in the later section. A quick evaluation of the grid size based on the analytical solution is thus suggested to perform before numerical simulations. For a specific reservoir simulation case, this grid size can be quantitatively determined given the simulation time step and the error tolerance of the distance ratio discussed above. Since the EDFM only introduces errors near the fracture in the space domain, i.e., grid blocks that are intersected by the fracture, we only need to refine these grids if the original grid-block size is too large, instead of applying the refined grid in the global reservoir domain.

3.3. Infinite and finite conductivity fracture

Infinite conductivity fractures refer to fractures with zero pressure drop along the fracture during production or infinite large fracture permeability, while finite conductivity fractures are those with nonzero pressure drop along the fracture. The assumption of infinite fracture conductivity is valid if the dimensionless fracture conductivity $F_{cd} = (k_f w_f)/(k_m x_f)$ is larger than 300 (Cinco-Ley and Fernando Samaniego, 1981). These two kinds of fractures are handled differently in this study. For the infinite-conductivity case, the fracture is represented by only one computational volume element, of which the volume is the total volume of the fracture (left one in Fig. 3). This computational volume element connects to many matrix grid blocks. Calculations of the area and distances for each connection are discussed above. In this way, the pressure inside the fracture is the same.

For the finite-conductivity case, the fracture is further gridded into a set of fracture elements, as shown in the right plot of Fig. 3. In addition to matrix-matrix connections and matrix-fracture connections, we have fracture-fracture connections as well. Fracture-fracture connections can be calculated geometrically by checking their shared edges. The effective intersection between the fracture and one grid block leads to one fracture element. Thus, each fracture element only connects to one matrix grid block or two (if the fracture plane is on the face of the grid box).

3.4. Multiple connected fractures

Discussion above is about the processing of a single discrete fracture. For cases with multiple discrete fractures, if these fractures do not intersect, they are embedded in matrix grids separately as the single fracture. Otherwise, if there are intersections, special treatments need to be made for grids containing intersections (grids intersected with more than one fractures). Our solutions for this part are explained using a 2D synthetic problem for simple illustration, as shown in the upper left part of Fig. 4. It includes two matrix blocks and three fractures. In this approach, multiple fracture segments intersected with the same grid are aggregated into one computational volume element. Thus, this problem is transferred into fluid flow among four computational volume elements (two matrix elements and two fracture elements). It includes one matrix-matrix, one fracture-fracture, and two matrix-fracture connections, as shown in the right part of Fig. 4. This transformation follows the same idea as the classical double-permeability model (Duguid and Lee, 1977). It will not introduce significant numerical discretization errors, because pressure drops among various jointed fracture segments inside one grid block (especially in a locally refined grid) are negligible given their short connecting distance and high conductivities.

Compared with other alternative treatment methods (Moinfar et al., 2014), this local fracture-segment aggregation method reduces efforts of geometric calculations. The matrix-matrix and fracture-fracture connections can be obtained straightforwardly. For the matrix-fracture connections, the connection area is the sum of all intersected polygon area. Unlike the distance for the single-fracture intersection, $d(i, j, k)$ is the distance from the point (i, j, k) to the nearest fracture.

$$d(i, j, k) = \min_{t=1:m} [\text{distance}(P_{i,j,k}, Fracture_t)] \tag{7}$$

where m is the number of fractures intersected with this matrix grid. The lower left plot in Fig. 4 shows the contour of this distance for two matrix-fracture connections in this problem.

4. Model verification

Based on foregoing discussions, the calculated geometric information can be immediately implemented into our simulator by taking the advantage of the IFD method. In our developed simulator, the component mass-balance equations are discretized in space with the IFD concept, in which the upstreaming weighting method is applied to the mobility term and the harmonic mean method for the transmissivity term. Time discretization is carried out with a first-order, backward, fully implicit finite-difference method (or backward Euler method). The discrete nonlinear equations are solved via the Newton iteration method (Wu et al., 2014; Wang and Wu, 2015; Xiong et al., 2015; Zhang et al., 2016). Three examples are designed, and several simulations are performed to examine the accuracy of the 3D-EDFM algorithm. The first example involves single 2D fracture; the second one contains multiple 2D connected fractures; and the third one is to study a 3D facture. Benchmark solutions include the approximate analytical solutions from the literature (the first example) and simulation results from two other established numerical approaches (the second and third example).

4.1. Single fracture

Fig. 5 shows a schematic diagram of the first case. The system contains a horizontal, infinite-acting, homogeneous, and isotropic

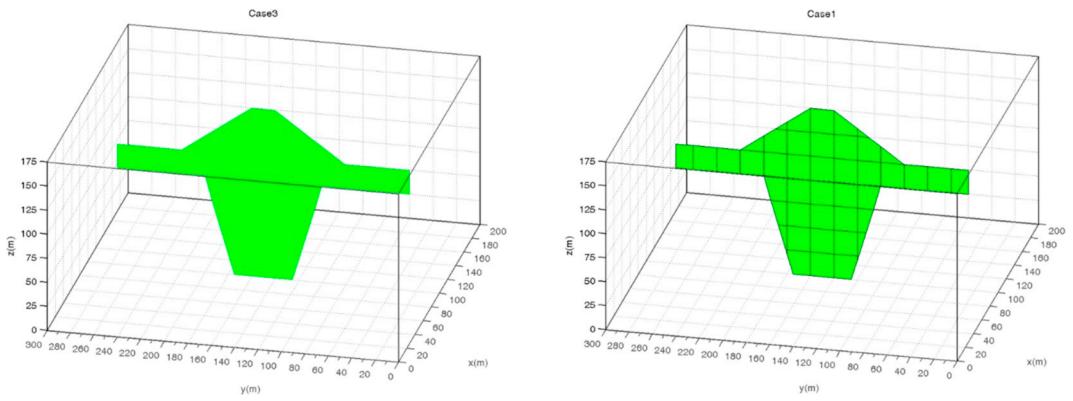

Fig. 3. Demonstrations of different numerical methods to handle infinite-conductivity fracture (left) and finite-conductivity fracture (right).

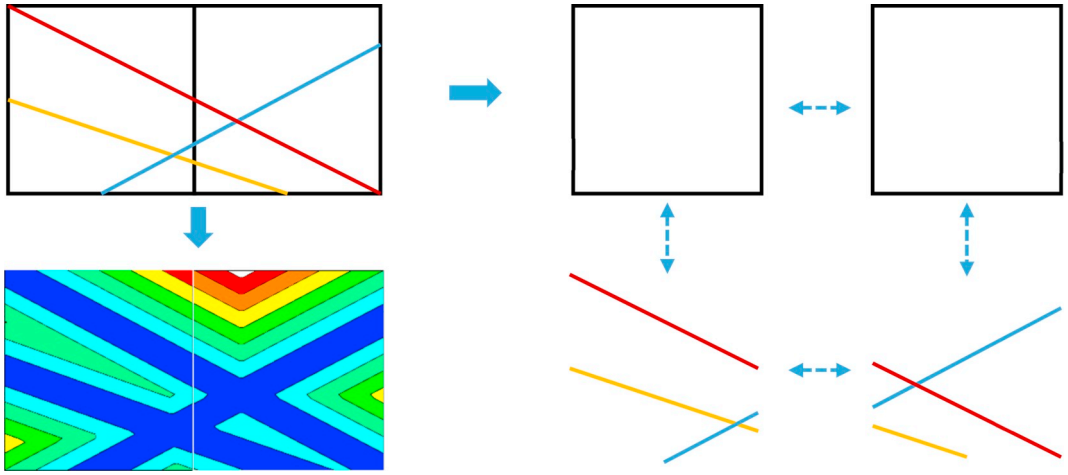

Fig. 4. Upper left: a 2D synthetic problem with two matrix blocks and three intersected fractures. Right: Numerical idealization for this problem, which includes two matrix elements and two fracture elements; Lower left: contour of distance for two matrix-fracture connections.

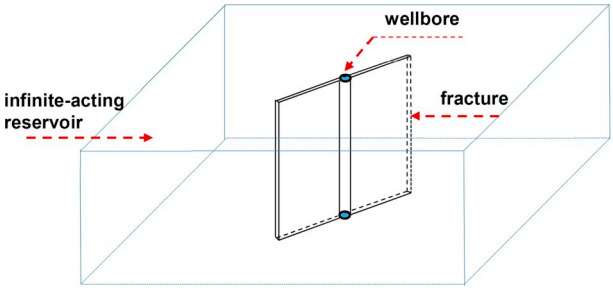

Fig. 5. Vertical fracture in an infinite slab reservoir.

formation. One vertical well and one vertical hydraulic fracture are put inside this reservoir. The plane of the hydraulic fracture includes the wellbore. It totally penetrates the reservoir formation in the vertical direction. A single-phase, slightly compressible fluid is produced from the well at constant rate. For the infinite fracture conductivity case, the pressure along hydraulic fractures remains equal to the bottom-hole pressure. For the finite fracture conductivity case, the fracture permeability is calculated based on the fracture conductivity value. Parameters are given in Table 1. Analytical solution of the well pressure with the infinite- and finite-conductivity fracture are given by Gringarten et al., (1974) and Cinco and Meng (Cinco-Ley and Fernando Samaniego, 1981; Cinco-Ley and Meng, 1988), respectively.

Fig. 6 presents comparisons between the numerical solutions and analytical (true) solutions with various fracture conductivities. It indicates from low conductivities (C_{fd} = 0.5) to high ones (C_{fd} = 10,000), all results from the EDFM are in good agreement with the analytical solution. In numerical models, the reservoir length and width are fifteen times of the fracture length to approximate the "infinite-acting" set-up. The minor discrepancy for some cases in the very early time is because the fracture volume in the analytical approach is set to be zero, while this volume should be given a non-zero value in the numerical approach.

Fig. 7 shows the sensitivity analysis of the EDFM with respect to the grid size. Comparison results from Fig. 7 indicate that numerical results are in good agreement with the analytical solution for this problem with a grid size of 1 m and 2 m. For the grid size of 5 m and 10 m, some discrepancies are observed when the dimensionless time is smaller than 0.2, which is 0.65s in real time for this problem. Numerical results are acceptable after this point of time. This discrepancy comes from the difference between transient state flow (real) and steady state flow (numerical approach assumption) inside the grids which contains fractures in the very early time. For most of the simulation cases, however, the interested time interval is far larger than this short time. In addition, this discrepancy can be eliminated if the local grids are refined with the 2 m grid, as shown in the case of the 10 m grid with 2 m LGR in Fig. 7.

Fig. 8 shows simulation results by rotating the vertical fracture with various angles. Two-meter grid is used for all these simulation cases. Though the fracture geometry (length, width, and height) in these cases stay the same, the number of intersected grids, intersection areas for various grids, and the average distance in these numerical cases are different. Simulation results are shown to be almost the same since the reservoir size is much larger than the fracture size. All these numerical simulation results are in good agreement with the analytical solution, which demonstrates the ability of the method to handle fractures with arbitrary directions.

4.2. Multiple fractures

This section examines the validity of EDFM to handle multiple connected fractures. A simple synthetic 2D model containing four fracture branches (28 fractures in total) is built as shown in Fig. 9. The infinite conductivity condition is assumed in this verification example. The initial reservoir pressure is 8000 psi, and this reservoir is under production with constant BHP control (2000 psi) for 30 months. For this problem, fractures are handled explicitly using three different approaches: the local grid refinement method, the unstructured grid method (triangular grids for 2D cases), and the EDFM (Fig. 10). The first two approaches are well established as discussed in section 1. Fig. 11 displays the simulation results for these cases. We observed that the EDFM results are nearly indistinguishable from the reference LGR and triangular grid methods.

In the problem, the EDFM shows a better computational efficiency

Table 1
Synthetic model parameters for numerical model verifications.

Parameters, Units	Values
Fracture half-length, m	5.00
Reservoir permeability, mˆ2	9.87E-16
Porosity	0.05
Fluid viscosity, Pa*S	8.90E-04
Total compressibility, 1/Pa	4.58E-10
Initial pressure, Pa	4.14E+07
Production rate, mˆ3/s	2.00E-06
Reservoir length, m	150
Reservoir width, m	150
Reservoir thickness, m	1.0

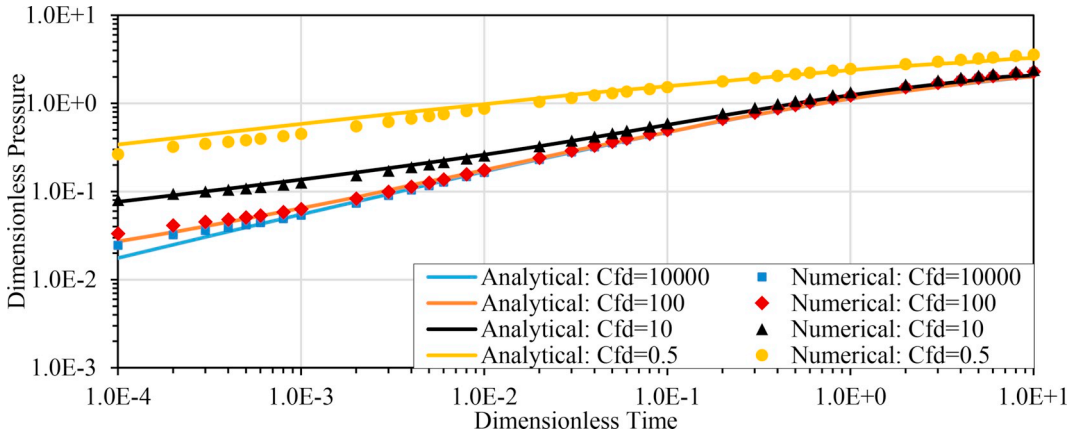

Fig. 6. Comparisons of wellbore pressure vs. time between the analytical solution ("Cinco-Samaniego" type curve), and numerical solution with various fracture conductivities (Cinco-Ley and Fernando Samaniego, 1981).

for the simulation. As shown in Table 2, the number of cells and connections for the EDFM is much less than other two methods. For this example, the EDFM provides about 15 times speed up relative to the reference LGR method and 3.6 times speed up relative to the triangular grid method. This enhanced performance results from the decrease of Jacobian matrix size and complexity. Solving the Jacobian matrix related linear algebra is the single-most time consuming part in reservoir simulation. As shown in Fig. 12, the LGR method leads to an irregular seven band sparse Jacobian matrix with the size of 10,120×10,120. The triangular grid method has a relatively dense matrix with the size of 6,800×6,800. The EDFM has a five diagonal band sparse Jacobian matrix with the size of 1,601×1,601, which has a similar sparsity pattern with the traditional simulation approach.

5. Application

The EDFM method is here applied to three problems that are of special interest in unconventional reservoirs. We present simulations results with (1) fractures with complicated shapes due to the multi-layer features and vertical heterogeneity, (2) multiple curved fractures due to the stress shadow effect, and (3) multiple arbitrary-direction fractures with complicated connections due to the hydraulic fracture and natural fracture interactions. The first problem is described in detail, and the other two are relatively illustrative. The major objective of these three examples is to demonstrate the capacity of the EDFM to capture all of the common phenomena related to complicated fractures in developing unconventional reservoirs. Note that single-phase flow is involved in most simulated cases, a two-phase flow is added into the third problem. The 3D-EDFM method can be directly applied for the first two cases with multi-phase fluid flow because gridding and handling fluid flow physics are two independent modules under our numerical scheme.

5.1. The multi-layer case

The hydraulic fracture shape in unconventional reservoir formations will most likely deviate from the classical, ideal bi-wing shape in conventional reservoirs (Zhou, 2016). This results from the multiple layer features or formation heterogeneity that are observed in many unconventional reservoirs (Passey et al., 2010; Donovan et al., 2012; Hart et al., 2013). Since the geomechanical and fracturing properties, such as elastic modulus, fracture toughness, and leak-off coefficients, vary distinctly among these layers, created hydraulic fracture widths and lengths in different layers are significantly different.

Fig. 13 (the left part) shows such a hydraulic fracture with complicated shapes from geomechanics simulations (Zhai and Fonseca, 2015; Geilikman et al. 2015). The color contour indicates local variations of the fracture width. As shown in the right part of Fig. 13, the reservoir containing this fracture is assumed to be rectangular with dimensions of 200 m × 300 m × 120 m. This is a closed-boundary reservoir. It is subdivided into regular grids of 1800 blocks with dimensions of 20 m × 20 m × 10 m. These grid blocks are visualized on the surfaces of the reservoir box.

The fracture is embedded into these regular grids, leading to 1899 computational grids (1800 matrix grids and 99 fracture grids), and 5239 computational connections (4950 matrix-matrix connections, 99

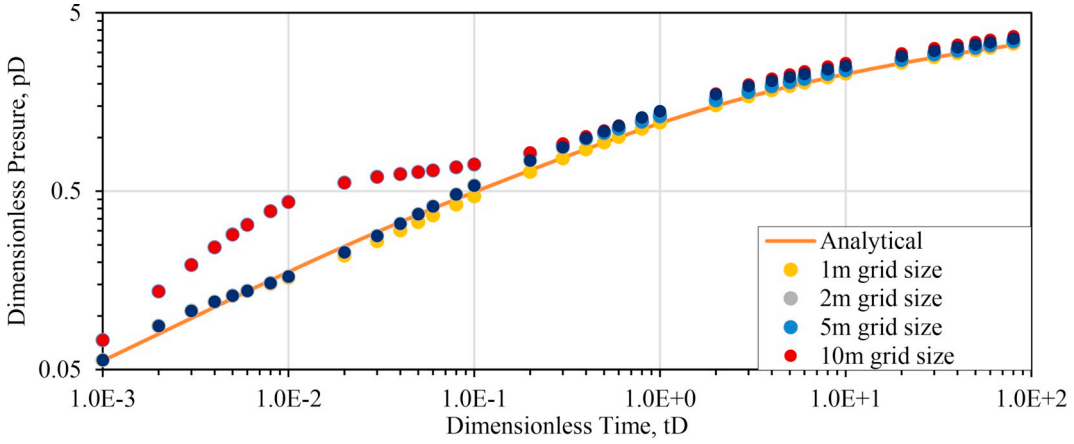

Fig. 7. Comparisons of wellbore pressure vs. time between the analytical solution, and numerical solution with various grid sizes for infinite fracture conductivity.

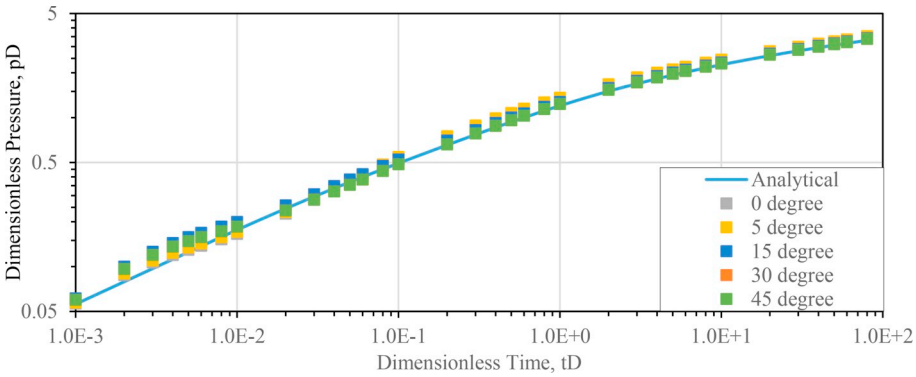

Fig. 8. Comparisons of wellbore pressure vs. time between the analytical solution, and numerical solution with various fracture orientation for infinite fracture conductivity.

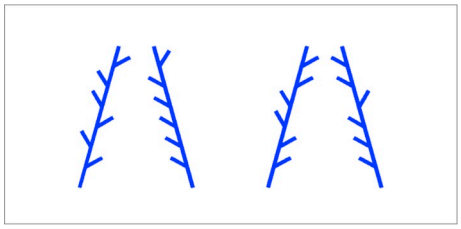

Fig. 9. Synthetic 2D model with 4 fracture branches.

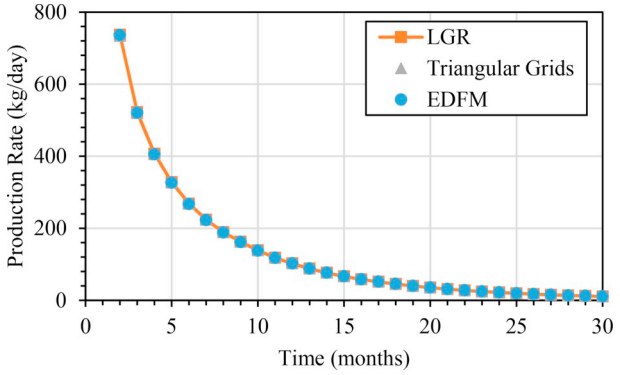

Fig. 11. Oil production rate results for three solutions for synthetic 2D flow.

matrix-fracture connections, and 190 fracture-fracture connections). The horizontal well connects with one fracture grid in the mid-lower part, as illustrated in the left part of Fig. 13.

In our simulation, the fracture permeability is correlated from the fracture width following the cubic law ($k_f = w_f^2/12$). The lateral reservoir permeability is given a value of 0.1mD. The vertical reservoir permeability is assumed to be one tenth of this value to account the layering effect. The estimation of the dimensionless fracture conductivity indicates that this fracture cannot be treated with infinite conductivities. The initial reservoir pressure is 6000 psi, and this reservoir is depleted with a constant BHP of 1000 psi. Fluids in this system are in the single phase with the viscosity of 1.0 cp and the compressibility of 4.58E-10 Pa^{-1}.

The lateral (y-z) view of the pressure distribution inside the fracture at 1.0 day is shown in Fig. 14, which indicates fluids within the fractures travels towards the wellbore. It has a pseudo-radial flow pattern close to the wellbore and a linear flow pattern away from the wellbore. This flow pattern is controlled by both the distance from the wellbore and the fracture shape.

Fluid flow inside the fracture is feed by fluids from the reservoir. Three layers (shown in Fig. 13) are selected to demonstrate our simulated flow patterns inside the reservoir. These three layers are penetrated with hydraulic fractures by different lengths. Fig. 15 shows the top (x-y) view of contour lines of pressure for these three layers at 10.0 days. For the first one, the fracture extends nearly to the reservoir drainage boundary. Our simulation results (the left one in Fig. 15) tell this layer of reservoir feeds the fractures via linear flow instead of pseudo-radial flow. It matches the analytical study in literature (Wattenbarger et al., 1998). For the second layer, in which the fracture

Table 2
Comparison of problem size and simulation times for these three approaches.

	Number of Cells	Number of Connections	Simulation Time (s)
LGR	10120	66482	435.16
Triangular Grids	6800	10480	101.55
EDFM	1601	8197	28.17

length is about one-third of the reservoir width, simulated contour lines inside can be described using elliptical geometry (the mid one in Fig. 15). This elliptical pattern of the propagating pressure transient matches the analytical solution by Hale and Evers, (1981). The third layer connects with two relatively short fracture segments. Simulated pressure contour lines can be described as two sets of ellipses with shorter focal lengths surrounded by one set of longer focal-length ellipses (the right one in Fig. 15). Furthermore, in this highly anisotropic reservoir, flow towards the hydraulic fracture is mainly along the horizontal direction, and there are little vertical flow crossing layers.

5.2. *The natural fracture interaction case*

The microseismic data may give some information on that the

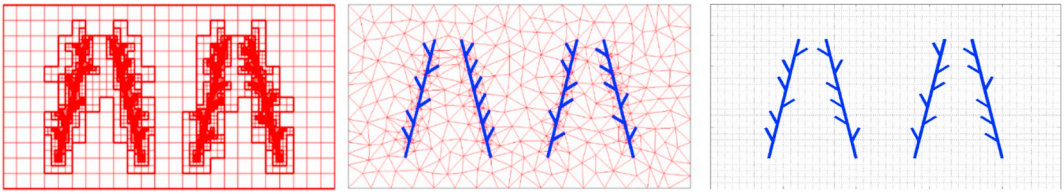

Fig. 10. Space discretization for three different fracture simulation methods (from left to right: LGR, triangular grids, and EDFM).

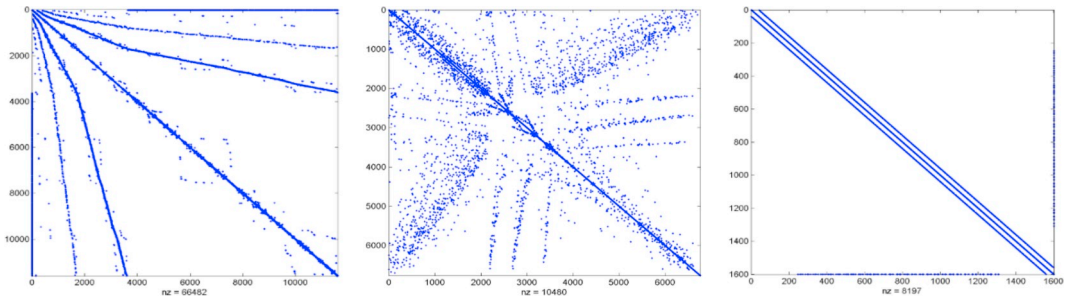

Fig. 12. Comparison of Jacobian matrix size and complexity of these three approaches (from left to right: LGR, triangular grids, and EDFM).

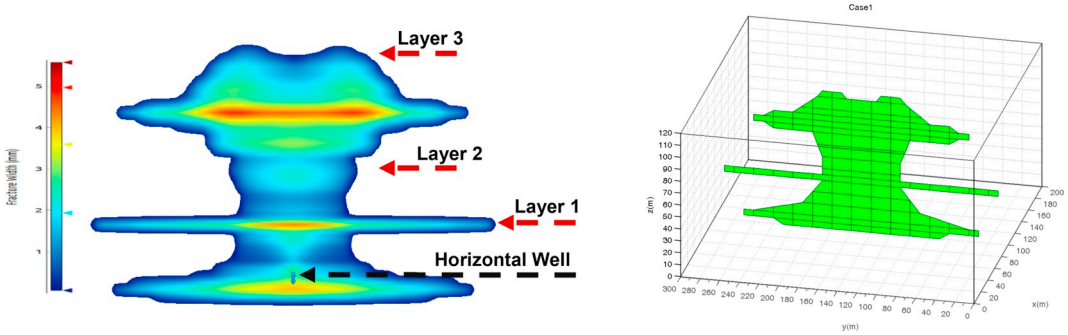

Fig. 13. Left: Illustrations of a hydraulic fracture with complicated shapes from geomechanics simulations. Three layers are selected to demonstrate our simulated flow patterns inside the reservoir. Right: Discretization grids for the reservoir and the embedded fracture.

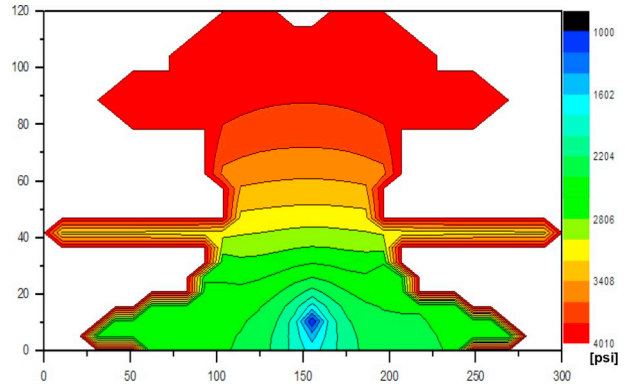

Fig. 14. The lateral (y–z) view of the pressure distribution inside the fracture at 1.0 day.

fracture shape involves not only a single isolated planar fracture, but also has irregular traces with a fractured zone around (Fisher and Warpinski, 2012; Geilikman et al. 2015). Small fractures in the fracture zone are originally natural fractures which are partly open or sealed under natural condition. The sealed fractures cannot contribute to permeability enhancement initially but act as planes of weakness and reactive during drilling or hydraulic fracturing (Gale et al., 2007; Olson and Taleghani 2009). Considering these complicated fracture geometries will improve simulation results in a more realistic and accurate way.

Fig. 16 shows three DFNs generated from the same set of microseismic data considering distance uncertainties by use of Hough transforms (Yu et al., 2016). These DFNs are extracted from figures in Yu's publication. Complexities of this fracture network come from interactions with natural fractures during hydraulic fracture propagation. In this problem, all activated fractures are assumed to be propped and act as effective high-conductivity pathways for fluid production.

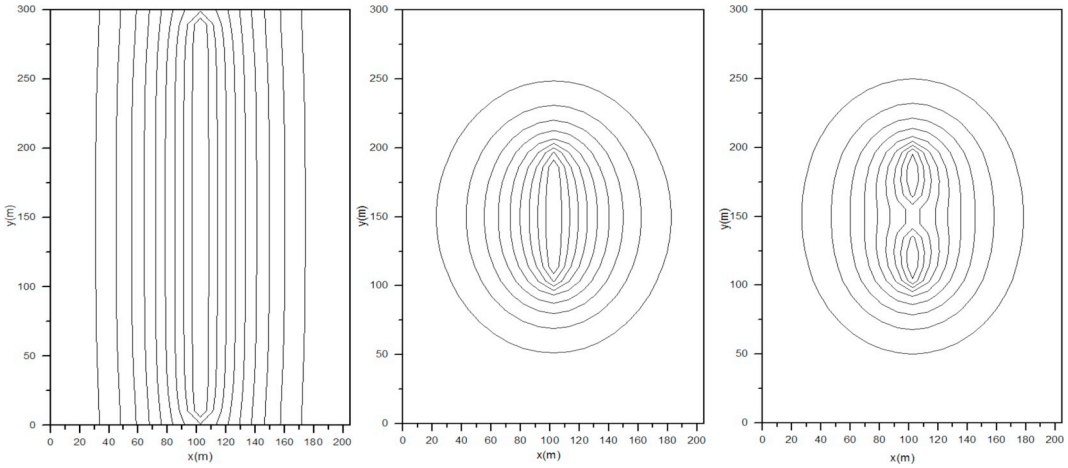

Fig. 15. The top (x–y) view of contour lines of pressure for these three layers at 10.0 days.

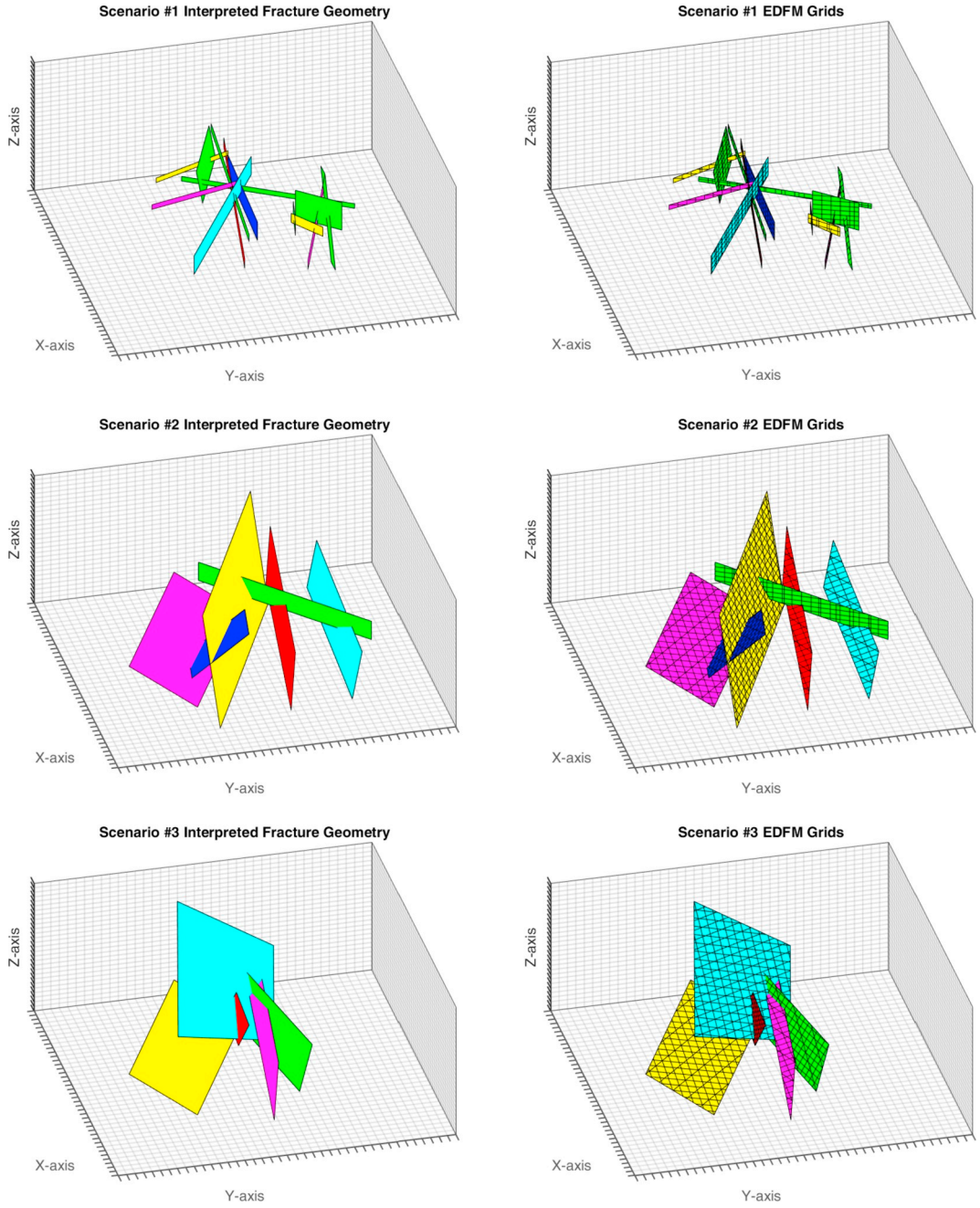

Fig. 16. Three DFN geometries extracted from Yu's paper (Yu et al., 2016) and corresponding 3D-EDFM grids (right).

Table 3
Information of the fracture geometry and EDFM gridding for these three cases.

Cases	Fracture Number	Fracture Area (m^2)	Fracture Connection Number		Fracture Grid Number			
			M-F	F-F	Trian	Quadra	Penta	Hexa
No. 1	13	100.3	707	1751	132	660	72	6
No. 2	6	225.7	1548	2931	602	516	483	35
No. 3	5	176.2	1125	2184	446	464	251	68

Fracture widths are given a uniform value of 0.01 m, and the effective fracture permeability is assumed to be $4.9345 \times 10^{-10} m^2$. Matrix permeabilities in three directions are $9.87 \times 10^{-18} m^2$. The reservoir under consideration is the area associated with only one stage of hydraulic fractures, which is a represented by a closed-boundary rectangle, $20m \times 20m \times 14m$ in extent. Grid dimensions are $0.5m \times 0.5m \times 0.5m$. All other simulation input parameters keep the same with the case in section 5.1. Note that the two-dimensional (or 2.5D) fracture handling approach is not applicable for this case, because most fractures are not aligned with grid axes. The 3D-EDFM discretization of these fractures leads to a combination of triangles, quadrilaterals, pentagons and hexagons. Details about the discretization results are listed in Table 3.

Two sets of reservoir simulation studies are conducted. The first involves single-phase fluid flow with these three DFNs. Fig. 17 presents horizontal slices of the simulated pressure-change contour for case 1 at 1,038s and 12,960s, which shows pressure depletion patterns with thirteen fractures are qualitatively captured. Quantitative analysis is presented in Fig. 18 and Fig. 19. Fig. 18 plots the simulated production rate vs. time in the log-log scale, following the routine of rate transient analysis (RTA). Simulation results indicate that linear fracture flow is

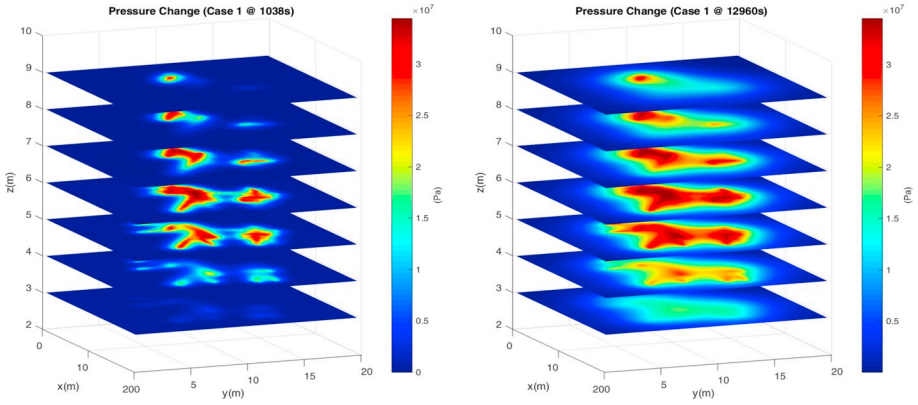

Fig. 17. Horizontal slices of simulated pressure contours for case 1 at 1038s (left) and 12,960s (right).

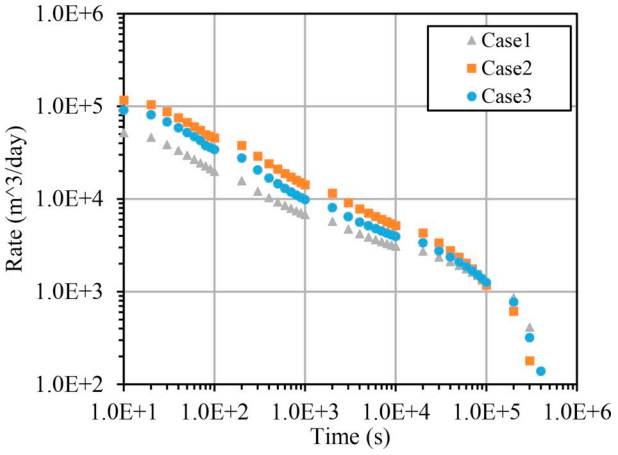

Fig. 18. Simulated production rate vs. time (log-log scale) for these three cases.

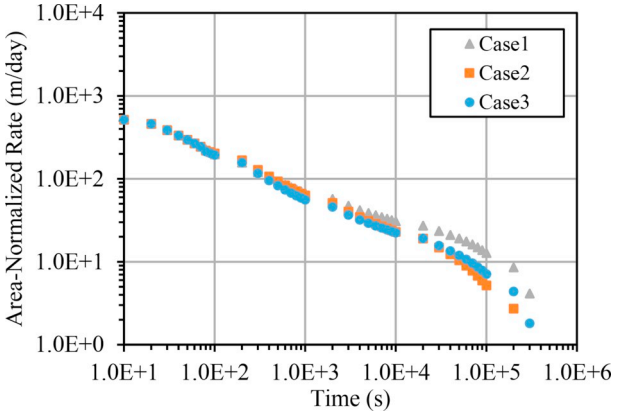

Fig. 19. Simulated area-normalized production rate vs. time (log-log scale).

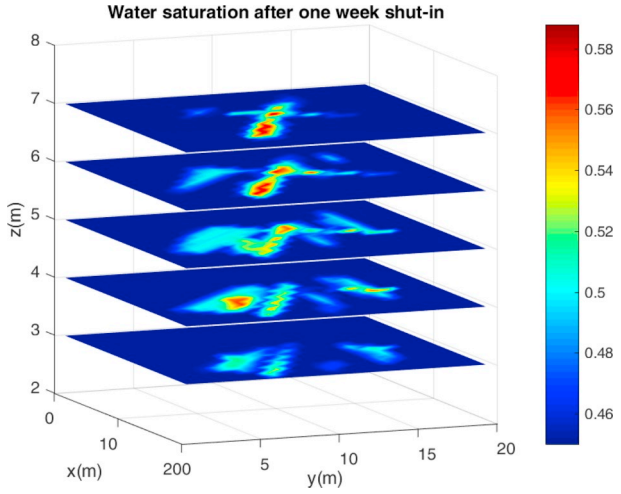

Fig. 20. Water saturation profiles after one-week well shut-in.

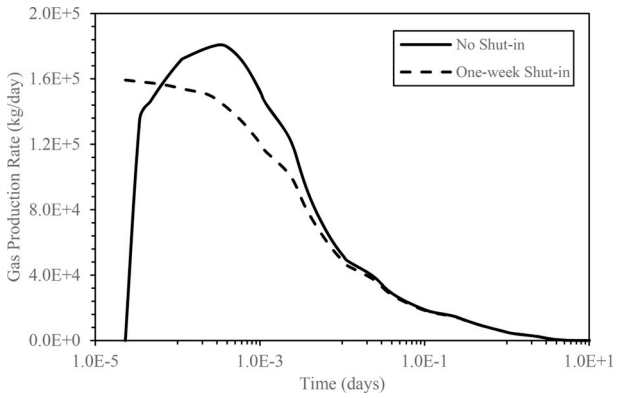

Fig. 21. Simulated gas production rate vs. time.

the dominate flow regime in the early time in these three cases (slopes of curves are close to $-1/2$), followed by a boundary dominated flow regime. This matches with physics, in turn, proves the effectiveness of the 3D-EDFM to handle complicated 3D fractures. Fig. 19 plots the area-normalized production rate (production rate divided by the total fracture area) vs. time. Fracture area data can be referred in Table 3. These three curves coincide in the early time, and this coincidence indicates that the most sensitive parameter of hydraulic fractures to early transient fluid flow through extremely low permeability matrix rock is the fracture-matrix contacting area, no matter how complicated the fracture geometry is. Based on this observation, it is possible to use rate transient testing data to estimate the effective area of fractures even for 3D complicated fractures.

Two-phase flow (gas and water) is also investigated using the DFN in case 2. Two simulation cases are designed to evaluate the impact of spontaneous imbibition or injection into matrix of fracturing fluids on post-fracturing production. In these two cases, the initial water saturation in matrix is set at the residual value (0.45), while the water saturation in fractures is 1.0. Initial pressure in matrix and fractures keep the same. The well is shut in for a while before turning on production with a constant BHP. Shut-in time varies in these two cases: no shut-in time in case 1 and one week in case 2. The simulated water saturation profile after one-week shut-in, with a range between 0.45 and 0.60, is shown in Fig. 20. Simulated gas production rate and

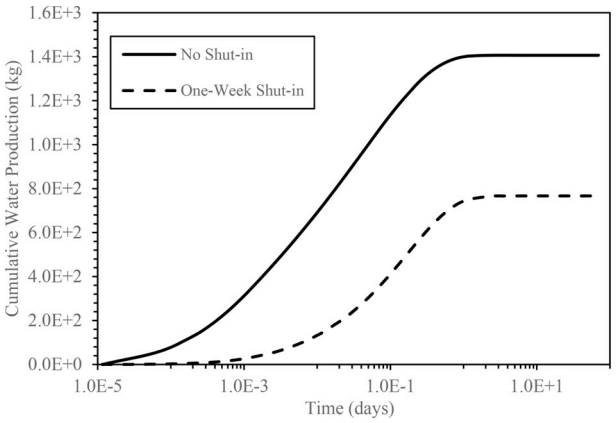

Fig. 22. Simulated cumulative water production vs. time.

accumulative water production from these two cases are presented in Fig. 21 and Fig. 22, respectively. From Fig. 21, the gas flow rate in case 2 is higher in the very early time. This is because most of the produced gas in this period is from fractures, and certain amounts of gas originally in matrix is displaced and flows into fractures by water imbibition during the shut-in (Fakcharoenphol et al., 2013). When gas produced from matrix becomes dominant, gas flow rate in case 1 becomes higher as the imbibed water forms a blockage by reducing the gas-phase relative permeability (Farah et al., 2017). From Fig. 22, the simulated cumulative water production from case 2 is only about 50% of that from case 1. This numerical simulation study supports observations from the field that typically only 10%–50% of fracturing fluids can be recovered (Zhou et al., 2014).

6. Conclusions

1. We present a 3D-EDFM method, which is applicable of modeling 3D complicated hydraulic fractures in reservoir simulation. The 3D-EDFM is generally able to handle 3D hydraulic fractures with arbitrary strike and dip angles, shapes, curvatures, conductivities, connections, and number of discrete fractures. In addition, it provides significant improvement in computational efficiency because of the decrease in Jacobian matrix size and the similarity in matrix sparsity pattern.

2. In the proposed 3D-EDFM, 3D complicated hydraulic fractures are handled by a geometric methodology in gridding for an unstructured-grid reservoir simulator. Our analysis indicates that the geometric-based parameters are reliable to represent flow-based parameters. With these preprocessed grid parameters, the 3D-EDFM can be directly implemented into reservoir simulators via the integral finite difference (IFD) method.

3. The 3D-EDFM is verified by comparison with the Gringarten analytical solution for fluid flow with a single fracture of infinite conductivity and arbitrary directions, with the Cinco-Samaniego type curves for fluid flow with a single fracture of finite conductivities, with two other DFM models for fluid flow with multiple connected fractures as well as with the LGR approach for 3D fractures.

4. The 3D-EDFM is flexible of handling hydraulic-fracture input data, as interpreted from geomechanics modelings as well as microseismic data. Several synthetic, but realistic testing cases are simulated. The 3D-EDFM captures key flow patterns qualitatively and quantitatively, inside both fractures and reservoirs, related to complicated fractures in these cases. For the layer in which the fracture extends nearly to the reservoir drainage boundary, fractures are feed via linear flow. For shorter fractures, pressure contour lines can be described using an elliptical geometry. In addition, the most sensitive parameter of hydraulic fractures to early transient fluid flow through extremely low permeability rock matrix is the fracture-matrix contacting area, no matter how complicated the fracture geometry is.

Acknowledgement

We thank Dr. Zhaoqin Huang and Dr. Zhengfu Pan for their insightful suggestions on this work. Thanks are also due to anonymous reviewers of this work for their constructive suggestions. This work was supported in part by EMG Research Center in Petroleum Engineering Department at Colorado School of Mines; by CNPC USA; by Chuanqiong Drilling Engineering Company; and by Foundation CMG.

Appendix A. General Analytical Solutions for 1D Fluid Flow with a Fracture

The governing equation of 1D fluid flow of a single-phase single-component slightly compressible fluid in a homogeneous porous medium can be expressed as:

$$\frac{\partial p}{\partial t} = \frac{k}{\varphi \mu c}\frac{\partial^2 p}{\partial x^2} \tag{B-1}$$

The corresponding initial conditions and boundary conditions (Dirichlet conditions on the left and Neumann conditions on the right) are:

$$p(x, 0) = p_i \tag{B-2}$$

$$p(0, t) = p_f, \quad p_f < p_i \tag{B-3}$$

$$\frac{\partial p}{\partial x}(x_L, t) = 0 \tag{B-4}$$

Introduce dimensionless variables

$$x_D = \frac{1}{x_L}x \tag{B-5}$$

$$t_D = \frac{k}{\varphi \mu c x_L^2}t \tag{B-6}$$

$$p_D = \frac{(p - p_f)}{p_i} \tag{B-7}$$

We have the dimensionless form of 1D fluid flow in porous medium governing equations as well as its boundary and initial conditions:

$$\frac{\partial p_D}{\partial t_D} = \frac{\partial^2 p_D}{\partial x_D^2} \tag{B-8}$$

$$p_D(x_D, 0) = \frac{(p_i - p_f)}{p_i} \tag{B-9}$$

$$p_D(0, t_D) = 0 \tag{B-10}$$

$$\frac{\partial p_D}{\partial x_D}(1, t_D) = 0 \tag{B-11}$$

Through the superposition principle (Gordon, 1989), the dimensionless analytical solution for this 1D fluid flow problem is

$$p_D(x_D, t_D) = \frac{2(p_i - p_f)}{p_i \pi} \sum_{n=1}^{\infty} \frac{1}{\left(n - \frac{1}{2}\right)} \sin\left[\left(n - \frac{1}{2}\right)\pi x_D\right] \exp\left(-(n - 0.5)^2 \pi^2 t_D\right) \tag{B-12}$$

Correspondingly, the analytical solution of pressure as a function of time and space is

$$p(x, t) = p_f + \frac{2(p_i - p_f)}{\pi} \sum_{n=1}^{\infty} \frac{1}{\left(n - \frac{1}{2}\right)} \sin\left[\left(n - \frac{1}{2}\right)\pi \frac{x}{x_L}\right] \exp\left(-(n - 0.5)^2 \pi^2 \frac{k}{\varphi \mu c x_L^2} t\right) \tag{B-13}$$

Production rate into the fracture can be derived based on Darcy's Law and Eq. (B-13):

$$q = A_f \frac{k}{\mu} \frac{\partial p}{\partial x}(0, t) = A_f \frac{k}{\mu} \frac{2(p_i - p_f)}{x_L} \sum_{n=1}^{\infty} \exp\left(-(n - 0.5)^2 \pi^2 \frac{k}{\varphi \mu c x_L^2} t\right) \tag{B-14}$$

The average pressure in the first grid (with the width of Δx_1) is obtained by the integration over this grid volume:

$$p_{ave}(0{:}\ \Delta x_1, t) = \frac{\int_0^{\Delta x_1} p(x,t) A_f dx}{A_f \Delta x_1}$$

$$= p_f + \frac{2x_L\left(p_i - p_f\right)}{\pi^2 \Delta x} \sum_{n=1}^{\infty} \frac{1}{(n - 0.5)^2}\left(1 - \cos\left[(n - 0.5)\pi \frac{\Delta x_1}{x_L}\right]\right) \exp\left(-(n - 0.5)^2 \pi^2 \frac{k}{\varphi \mu c x_L^2} t\right) \tag{B-15}$$

For our simulation, discretized Darcy's law for the first grid is

$$q = A_f \frac{k}{\mu} \frac{p_{ave}(0{:}\ \Delta x_1, t) - p(0, t)}{d_{m-f}} \tag{B-16}$$

Thus, the equivalent average matrix-fracture distance in the first grid

$$d_{m-f} = \frac{p_{ave}(0 : \Delta x_1, t) - p(0, t)}{A_f \frac{k}{\mu} Q}$$

$$= \frac{x_L^2 \sum_{n=1}^{\infty} \frac{1}{(n - 0.5)^2}\left(1 - \cos\left[(n - 0.5)\pi \frac{\Delta x_1}{x_L}\right]\right) \exp\left(-(n - 0.5)^2 \pi^2 \frac{k}{\varphi \mu c x_L^2} t\right)}{\Delta x_1 \pi^2 \sum_{n=1}^{\infty} \exp\left(-(n - 0.5)^2 \pi^2 \frac{k}{\varphi \mu c x_L^2} t\right)} \tag{B-17}$$

Appendix B. Analytical Solutions of 1D Fluid Flow with a Fracture Under Steady or Pseudo-Steady State

The governing equation of 1D fluid flow of a single-phase single-component slightly compressible fluid in a homogeneous porous medium can be expressed as:

$$\frac{\partial p}{\partial t} = \frac{k}{\varphi \mu c} \frac{\partial^2 p}{\partial x^2} \tag{C-1}$$

When fluids flow in this 1D reservoir reaches pseudo-steady state, the rate of pressure drop at each point is the same:

$$\frac{\partial p}{\partial t} = C \tag{C-2}$$

Substituting Eq. (C-2) into Eq. (C-1), we have:

$$\frac{\partial^2 p}{\partial x^2} = \frac{\varphi \mu c}{k} C = B_1 \tag{C-3}$$

The general solution for differential equation Eq. (C-3) is

$$p(x, t) = \frac{B_1}{2} x^2 + B_2 x + B_3 + Ct \tag{C-4}$$

where B_1, B_2, B_3 and C are four constants.

The partial derivative of p with respect to x from Eq. (C-4) is

$$\frac{\partial p}{\partial x} = B_1 x + B_2 \tag{C-5}$$

At the right boundary, the pressure derivative is zero with the definition of pseudo-steady state:

$$\frac{\partial p}{\partial x}(x_L, t) = B_1 x_L + B_2 = 0 \tag{C-6}$$

Pressure at the left boundary is the fracture pressure:

$$p(0, t) = B_3 + Ct = p_f \tag{C-7}$$

Another boundary condition on the left is based on Darcy's law:

$$\frac{\partial p}{\partial x}(0, t) = B_2 = \frac{q\mu}{kA_f} \tag{C-8}$$

Combining Eq. (C-6) and Eq. (C-8), we have:

$$B_1 = -\frac{q\mu}{kA_f x_L} \tag{C-9}$$

The average pressure in the first grid (with the width of Δx_1) is obtained by the integration over this grid volume:

$$p_{ave}(0{:}\ \Delta x_1, t) = \frac{\int_0^{\Delta x_1} p(x, t) A_f dx}{A_f \Delta x_1} = \frac{B_1}{6}\Delta x_1^2 + \frac{B_2}{2}\Delta x_1 + P_f \tag{C-10}$$

Substitute Eq. (C-8) and Eq. (C-9) into Eq. (C-10), we have:

$$p_{ave}(0{:}\ \Delta x_1, t) - p_f = \left(-\frac{\Delta x_1}{3x_L} + 1\right)\frac{q\mu}{kA_f}\frac{\Delta x_1}{2} \tag{C-11}$$

In Eq. (C-11), the ratio of Δx_1 (in the grid-size scale) and x_L (in the reservoir-size scale) is typically very small. Thus, the first term inside the bracket is negligible. By reformulating Eq. (C-11), we can obtain the equivalent average matrix-fracture distance in the first grid:

$$d_{m-f} = \frac{p_{ave}(0{:}\ \Delta x_1, t) - p(0, t)}{A_f \frac{k}{\mu} Q} = \frac{\Delta x_1}{2} \tag{C-12}$$

For the steady-state flow, the constant C in Eq. (C-2) becomes zero. The constant B_1 becomes zero correspondingly. In addition, the boundary condition on the right changes from Neumann conditions to Dirichlet conditions. Following the same procedure, we can obtain that the equivalent average matrix-fracture distance for the steady-state flow in the first grid is also half of the grid size.

References

Cai, Long, Ding, Didier-Yu, Wang, Cong, Wu, Yu-Shu, 2015. "Accurate and efficient simulation of fracture–matrix interaction in shale gas reservoirs. Transport Porous Media 107 (2), 305–320. https://doi.org/10.1007/s11242-014-0437-x.

Cinco-Ley, H., Meng, H.-Z., 1988. In: Pressure Transient Analysis of Wells with Finite Conductivity Vertical Fractures in Double Porosity Reservoirs. Society of Petroleum Engineers. https://doi.org/10.2118/18172-MS.

Cinco-Ley, Heber, Fernando Samaniego, V., 1981. Transient pressure analysis for fractured wells. J. Pet. Technol. 33 (09), 1749–1766. https://doi.org/10.2118/7490-PA.

Ding, Didier Yu, Wu, Y.-S., Farah, Nicolas, Wang, Cong, Bernard, Bourbiaux, 2014. Numerical simulation of low permeability unconventional gas reservoirs. In: SPE/EAGE European Unconventional Resources Conference and Exhibition, . http://www.earthdoc.org/publication/publicationdetails/?publication=75116.

Donovan, Arthur D., Scott Staerker, T., Pramudito, Aris, Li, Weiguo, Corbett, Matthew J., Christopher, M., Lowery, Andrea, Romero, Miceli, Gardner, Rand D., 2012. The eagle ford outcrops of west Texas: a laboratory for understanding heterogeneities within unconventional mudstone reservoirs. http://archives.datapages.com/data/gcags-journal/data/001/001001/pdfs/162.htm.

Duguid, James O., Lee, P.C.Y., 1977. Flow in fractured porous media. Water Resour. Res. 13 (3), 558–566. https://doi.org/10.1029/WR013i003p00558.

Fakcharoenphol, Perapon, Ali Torcuk, Mehmet, Wallace, Jon, Antoine, Bertoncello, Kazemi, Hossein, Wu, Yu-Shu, Honarpour, Matt, others, 2013. Managing shut-in time to enhance gas flow rate in hydraulic fractured shale reservoirs: a simulation study. In: SPE Annual Technical Conference and Exhibition. Society of Petroleum Engineers. https://www.onepetro.org/conference-paper/SPE-166098-MS.

Farah, Nicolas, Ding, Didier-Yu, Wu, Yu-Shu, 2017. Simulation of the impact of fracturing-fluid-induced formation damage in shale gas reservoirs. SPE Reservoir Eval. Eng. 20 (03), 532–546. https://doi.org/10.2118/173264-PA.

Fisher, M. Kevin, Warpinski, Norman R., 2012. Hydraulic-fracture-height growth: real data. SPE Prod. Oper. 27 (01), 8–19. https://doi.org/10.2118/145949-PA.

Gale, Julia F.W., Reed, Robert M., Holder, Jon, 2007. Natural fractures in the barnett shale and their importance for hydraulic fracture treatments. AAPG (Am. Assoc. Pet. Geol.) Bull. 91 (4), 603–622. https://doi.org/10.1306/11010606061.

Gordon, N. Ellison, 1989. Thermal Computations for Electronic Equipment. Robert Krieger Publishing Co., Malabar, FL.

Gringarten, Alain C., Henry, J.Ramey, Raghavan, R., 1974. Unsteady-state pressure distributions created by a well with a single infinite-conductivity vertical fracture. Soc. Petrol. Eng. J. 14 (04), 347–360. https://doi.org/10.2118/4051-PA.

Hale, Brent W., Evers, J.F., 1981. Elliptical flow equations for vertically fractured gas wells. J. Pet. Technol. 33 (12), 2489–2497. https://doi.org/10.2118/8943-PA.

Hart, B., Macquaker, J., Taylor, K., 2013. "Mudstone ('Shale') depositional and diagenetic processes: implications for seismic analyses of source-rock reservoirs. Interpretation 1 (1) B7–26. https://doi.org/10.1190/INT-2013-0003.1.

Hui, Mun-Hong, Gong, Bin, Karimi-Fard, Mohammad, Louis, J., Durlofsky, 2007. Development and application of new computational procedures for modeling miscible gas injection in fractured reservoirs. Soc. Petroleum Eng. https://doi.org/10.2118/109686-MS.

Karimi-Fard, M., Durlofsky, L.J., Aziz, K., 2004. An efficient discrete-fracture model applicable for general-purpose reservoir simulators. SPE J. 9 (02), 227–236. https://doi.org/10.2118/88812-PA.

Kazemi, H., 1969. Pressure transient analysis of naturally fractured reservoirs with uniform fracture distribution. Soc. Petrol. Eng. J. 9 (04), 451–462. https://doi.org/10.2118/2156-A.

Lee, S.H., Lough, M.F., Jensen, C.L., 2001. Hierarchical modeling of flow in naturally fractured formations with multiple length scales. Water Resour. Res. 37 (3), 443–455. https://doi.org/10.1029/2000WR900340.

Li, Liyong, Lee, Seong H., 2008. Efficient field-scale simulation of black oil in a naturally fractured reservoir through discrete fracture networks and homogenized media. SPE Reservoir Eval. Eng. 11 (04), 750–758. https://doi.org/10.2118/103901-PA.

Moinfar, Ali, Varavei, Abdoljalil, Sepehrnoori, Kamy, Johns, Russell T., 2014. Development of an efficient embedded discrete fracture model for 3D compositional reservoir simulation in fractured reservoirs. SPE J. 19 (02), 289–303. https://doi.org/10.2118/154246-PA.

Narasimhan, T.N., Witherspoon, P.A., 1976. An integrated finite difference method for analyzing fluid flow in porous media. Water Resour. Res. 12 (1), 57–64. https://doi.org/10.1029/WR012i001p00057.

Neuman, Shlomo P., 2005. Trends, prospects and challenges in quantifying flow and transport through fractured rocks. Hydrogeol. J. 13 (1), 124–147. https://doi.org/10.

1007/s10040-004-0397-2.
Olson, Jon Edward, Taleghani, Arash Dahi, 2009. In: Modeling Simultaneous Growth of Multiple Hydraulic Fractures and their Interaction with Natural Fractures. Society of Petroleum Engineers. https://doi.org/10.2118/119739-MS.
Passey, Quinn R., Bohacs, Kevin, Lee Esch, William, Klimentidis, Robert, Sinha, Somnath, 2010. In: From Oil-Prone Source Rock to Gas-producing Shale Reservoir - Geologic and Petrophysical Characterization of Unconventional Shale Gas Reservoirs. Society of Petroleum Engineers. https://doi.org/10.2118/131350-MS.
Peaceman, D.W., 1978. Interpretation of well-block pressures in numerical reservoir simulation(includes associated paper 6988). Soc. Petrol. Eng. J. 18 (03), 183–194. https://doi.org/10.2118/6893-PA.
Pruess, Karsten, 1985. A practical method for modeling fluid and heat flow in fractured porous media. Soc. Petrol. Eng. J. 25 (01), 14–26. https://doi.org/10.2118/10509-PA.
Pruess, Karsten, Oldenburg, C.M., Moridis, G.J., 1999. TOUGH2 User's Guide Version 2. Lawrence Berkeley National Laboratory. http://escholarship.org/uc/item/4df6700h.pdf.
Rubin, Barry, 2010. In: Accurate Simulation of Non Darcy Flow in Stimulated Fractured Shale Reservoirs. Society of Petroleum Engineers. https://doi.org/10.2118/132093-MS.
Sadrpanah, Hooman, Charles, Thierry, Fulton, Jonathan, 2006. In: Explicit Simulation of Multiple Hydraulic Fractures in Horizontal Wells. Society of Petroleum Engineers. https://doi.org/10.2118/99575-MS.
Slough, K.J., Sudicky, E.A., Forsyth, P.A., 1999. Grid refinement for modeling multiphase flow in discretely fractured porous media. Adv. Water Resour. 23 (3), 261–269. https://doi.org/10.1016/S0309-1708(99)00009-3.
Sun, Jianlei, Schechter, David Stuart, 2014. In: Optimization-based Unstructured Meshing Algorithms for Simulation of hydraulically and Naturally Fractured Reservoirs with Variable Distribution of Fracture Aperture, Spacing, Length and Strike. Society of Petroleum Engineers. https://doi.org/10.2118/170703-MS.
Wang, Cong, 2013. Pressure Transient Analysis of Fractured Wells in Shale Reservoirs. COLORADO SCHOOL OF MINES. http://gradworks.umi.com/15/44/1544672.html.
Wang, Cong, Wu, Yushu, 2015. Characterizing hydraulic fractures in shale gas reservoirs using transient pressure tests. Petroleum 1 (2), 133–138. https://doi.org/10.1016/j.petlm.2015.05.002.
Warren, J.E., Root, P.J., 1963. The behavior of naturally fractured reservoirs. Soc. Petrol. Eng. J. 3 (03), 245–255. https://doi.org/10.2118/426-PA.
Wattenbarger, Robert A., El-Banbi, Ahmed H., Villegas, Mauricio E., Bryan Maggard, J., 1998. In: Production Analysis of Linear Flow into Fractured Tight Gas Wells. Society of Petroleum Engineers. https://doi.org/10.2118/39931-MS.
Wu, Y.S., 1998. MSFLOW: Multiphase Subsurface Flow Model of Oil, Gas and Water in Porous and Fractured Media with Water Shut-Off Capability, DOCUMENTATION and User's Guide. *Twange Int.*, Houston, Tex., Walnut Creek, Calif.
Wu, Yu-Shu, 2002. Numerical simulation of single-phase and multiphase non-Darcy flow in porous and fractured reservoirs. Transport Porous Media 49 (2), 209–240. https://doi.org/10.1023/A:1016018020180.
Wu, Yu-Shu, Li, Jianfang, Ding, Didier, Wang, Cong, Yuan, Di, others, 2014. A generalized framework model for the simulation of gas production in unconventional gas reservoirs. SPE J. 19 (05), 845–857.
Wu, Yu-Shu, Pruess, Karsten, 1988. A multiple-porosity method for simulation of naturally fractured Petroleum reservoirs. SPE Reservoir Eng. 3 (01), 327–336. https://doi.org/10.2118/15129-PA.
Xiong, Yi, Winterfeld, Philip H., Wang, Cong, Wu, Yu-Shu, Huang, Zhao-Qin, others, 2015. A compositional model fully coupled with geomechanics for liquid-rich shale and tight oil reservoir simulation. In: SPE Reservoir Simulation Symposium. Society of Petroleum Engineers. https://www.onepetro.org/conference-paper/SPE-173261-MS.
Yan, Xia, Huang, Zhaoqin, Yao, Jun, Yang, Li, Fan, Dongyan, 2016. An efficient embedded discrete fracture model based on mimetic finite difference method. J. Pet. Sci. Eng. 145 (September), 11–21. https://doi.org/10.1016/j.petrol.2016.03.013.
Yu, Xin, Jim, Rutledge, Scott, Leaney, Maxwell, Shawn, 2016. Discrete-fracture-network generation from microseismic data by use of moment-tensor- and event-location-constrained Hough transforms. SPE J. 21 (01), 221–232. https://doi.org/10.2118/168582-PA.
Zhai, Zongyu, Fonseca, Ernesto, 2015. History Match Case Study with a Multi-Cluster & Multi-Well Hydraulic Fracture Modeling Tool. http://archives.datapages.com/data/urtec/2015/2153981.htm.
Zhang, Ronglei, Yin, Xiaolong, Winterfeld, Philip H., Wu, Yu-Shu, 2016. A fully coupled thermal-hydrological-mechanical-chemical model for CO2 geological sequestration. J. Nat. Gas Sci. Eng. 28 (January), 280–304. https://doi.org/10.1016/j.jngse.2015.11.037.
Zhou, Jing, 2016. Hydraulic Fracture Propagation Modeling and Data-Based Fracture Identification. Ph.D.. The University of Utah, United States – Utah. http://search.proquest.com/docview/1803936953/abstract/A26A78B0038349D6PQ/1.
Zhou, Zhou, Hoffman, B. Todd, Bearinger, Doug, Li, Xiaopeng, 2014. In: Experimental and Numerical Study on Spontaneous Imbibition of Fracturing Fluids in Shale gas Formation. Society of Petroleum Engineers. https://doi.org/10.2118/171600-MS.